Mechanical Behavior at Finite Strain of Coalesced Core/Shell Latex Films

S. Lepizzera,† T. Pith,* C. Fond, and M. Lambla

Institut Charles Sadron (CRM-EAHP), 4 rue Boussingault, F-67083 Strasbourg Cédex, France

Received May 20, 1996; Revised Manuscript Received April 25, 1997[⊗]

ABSTRACT: Uniaxial deformation at finite strain of coalesced core/shell (hard core/film-forming shell) latex films is investigated by means of micromechanical calculations. Elongation ratios, strain rate, and energy density distribution within the film are presented and confirm the strain amplification phenomenon well-known in the filled elastomer area. The important role of the core−shell interphase on the overall film mechanical behavior is stressed by the presented results. Moreover, strain−stress curves have been calculated without adjustable parameters and compared to experimental ones in order to gain substantial information about the deformation mechanism. It is then proposed that uniaxial deformation of coalesced core/shell latex films proceed through two simultaneous and/or successive mechanisms: isotropic matrix deformation and geometrical core rearrangement within the film. The stiffening of coalesced core/shell latex films appears therefore to be mainly due to mechanical effects.

I. Introduction

Because volatile organic compounds have to be avoided as much as possible for ecological reasons, water-based coatings are becoming extensively used. Therefore, increasing research projects have been directed toward coalesced latex films. It is well established that low T_g polymer-based latexes are better film-forming material than high T_g ones. However, the lower the polymer T_g, the poorer the material mechanical behavior will be. Coalesced latex films with reasonable mechanical properties may be obtained, for instance,[1] with high T_g (glassy state) polymer core and film-forming polymer shell particles. The resulting film is then equivalent to a biphasic material having an elastomeric matrix with regularly distributed high modulus inclusions.

To date, most of the mechanical studies dealing with biphasic polymer materials have been devoted to rubber-modified thermoplastics, which are in some ways the opposite of filled elastomers. Moreover, while studies on mechanical behavior at small strain may be applied to both types of biphasic polymer materials,[2] at finite strain no general model has been devised. Mullins and Tobin[3] have proposed the first calculations intended to model the mechanical behavior at finite strain of filled elastomer using the mechanical behaviors of each phase. Because the modulus increase in the filled elastomer arises from "distortion of the stress pattern in the rubber matrix" and "absence of deformation in the filler", they proposed to relate the mean local strain experienced by the rubber phase to the overall strain of the sample by a strain-amplification factor greater than 1 (strain amplification phenomenon). However, based on that approach, no detailed information is available on the elongation ratio, strain rate, and energy density distributions within the filled elastomer. Moreover, these questions have not been addressed by more recent publications[4,5] concerning the mechanical properties of filled elastomers.

In the present contribution, the mechanical behavior at finite strain of coalesced core/shell latex films has been investigated through mechanical simulation, the main objective being to thoroughly understand the deformation mechanism of these biphasic films. Indeed, one has to determine if stiffening of coalesced core/shell latex films is due to mechanical or physico-chemical stiffening. For instance, it is well-known that the reinforcement of natural rubber by the carbon black particles is mainly due to the physico-chemical effects.

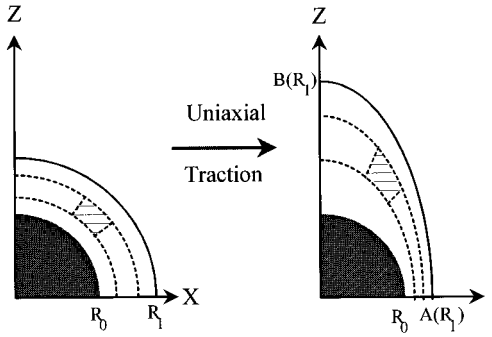

Figure 1. Elementary cell before and after uniaxial elongation used with the micromechanical model.

II. Micromechanical Calculations

Model Development. Latex film formation is admitted to proceed through three successive stages, namely water evaporation, particle coalescence, and aging.[6] After the first stage, it is assumed that particles are packed according to the face-centered cubic structure (fcc)[7] because it is the most efficient way of packing spheres. However, it has been recently[8] shown that the body-centered cubic (bcc) structure can also be observed in coalesced latex films. When film formation is complete, each particle in an fcc array and in a bcc array is deformed into a rhombic dodecahedron and into a tetrakaidecahedron, respectively. Dealing with coalesced core/shell latex films, these structures will have the "hard" core at their center. Because a rhombic dodecahedron and a tetrakaidecahedron are close to a sphere in the geometrical point of view, the elementary cell used for calculations is as depicted in Figure 1.

This elementary cell is based on an undeformable sphere surrounded by an elastomeric spherical shell, the two radii being calculated from the core volume fraction

* To whom correspondence should be addressed.
† Present address: ELF ATOCHEM, CRDE, Saint Avold, France.
⊗ Abstract published in *Advance ACS Abstracts,* November 1, 1997.

S0024-9297(96)00729-2 CCC: $14.00

(ϕ). Moreover, the interphase between the latex particle core and the shell is not considered since its nature and its mechanical behavior are unknown. However, perfect adhesion (neither debounding nor cavitation) is assumed between the elementary cell core and shell. Upon uniaxial traction, each elementary cell of the coalesced core/shell latex films is assumed to be deformed the same way. By calculating the deformation energy of the unique cell, the material's overall mechanical behavior may be estimated. In order to take into account the interaction between neighboring cells, it is assumed that uniaxial deformation of a spherical cell leads to an elliptical cell, whose principal axis is parallel with the deformation direction (Figure 1). The maximum extension ratio for these calculations is obviously reached when the outer bound of the shell touches the inner core. At this stage, it is expected that the material would undergo a mechanical transition; i.e., the kinematics of the deformation would have to change since the rigid cores remain almost spherical. Indeed, since the elementary cell core is based on a glassy state polymer and the shell on a rubbery state polymer, it can be assumed that the elementary cell core is not deformed during the traction experiment and that the elementary cell shell is deformed at constant volume.[9] Eventually, with the strain field in the shell and the strain-energy function of shell polymer, the mechanical behavior of the coalesced core/shell latex film may be estimated. In addition, the strain corresponding to the massive rearrangement of the cells may also be estimated.

The strain field is obtained using two additional and reasonable hypotheses. Firstly, it is assumed that spherical slices of the elementary cell shell become elliptic after uniaxial elongation. Secondly, slices can be divided into several torai that keep their volume constant during the traction experiment. Let us define $A(R)$ and $B(R)$ as the principal axes of an elliptical slice that was spherical with radius R in the undeformed state. Using the volume conservation hypothesis, it is easy to get the following relation between $A(R)$ and $B(R)$:

$$B(R)\,A(R)^2 = R^3 \tag{1}$$

The boundary conditions give additional relations:

$$B(R_0) = R_0 \tag{2}$$

$$B(R_1) = \lambda R_1 \tag{3}$$

where λ is the macroscopic cell extension ratio and $\lambda \in [1; (R_1/R_0)^2]$, R_0 is the core radius of the elementary cell, and R_1 is the elementary cell radius before deformation.

In order to find the strain field, the last problem to be solved is to know the function $A(R)$, which has to satisfy the following conditions:

$$A(R_1) = R_1/\sqrt{\lambda} \tag{4}$$

$$A(R_0) = R_0 \tag{5}$$

$$\frac{dA}{dR}(R_0) = 1 \tag{6}$$

$$\frac{dA}{dR}(R) \geq 0 \qquad \text{with} \qquad R \in [R_0; R_1] \tag{7}$$

Conditions 5 and 6 indicate simply that there is perfect adhesion between the core and shell. Since the core is supposed to be undeformable, the shell bound to it will experience almost no deformation during the experiment. Condition 7 is necessary in order to avoid overlapping of slices. Eventually, for the sake of simplicity, $A(R)$ should be a function having only one parameter in order to be easily optimized, as explained later. If one takes $A(R)$ as a third-order polynomial function of $R - R_0$, it can be shown that condition 7 is not fulfilled in the overall range of λ.

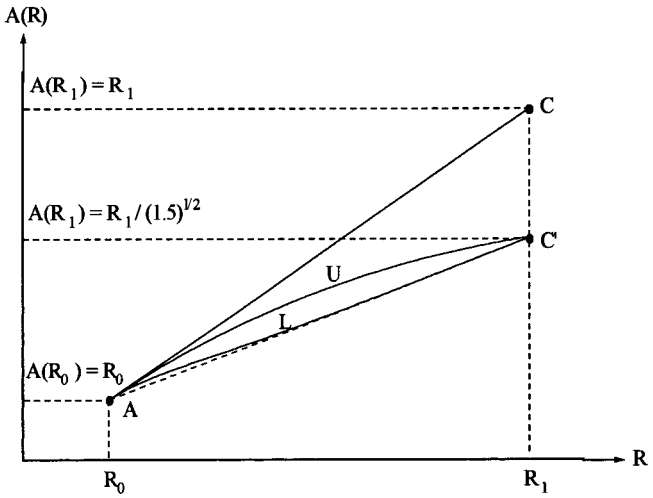

Figure 2. Example plot of $A(R)$ for $\phi = 0.2$, $\lambda = 1$, and $\lambda = 1.5$.

Figure 2 presents an example of an $A(R)$ plot. Before any deformation $A(R)$ is represented by the straight line between points A and C. When the elementary cell is stretched along its Z-axis, $A(R)$ becomes unknown but goes from points A to C′. Two extreme ways may then be used to do so. The first one is AUC′, which corresponds to almost no deformation of the smaller radius slices and high deformation of higher radius slices. The second one is ALC′, which corresponds to small deformation of the higher radius slices and high deformation of smaller radius slices. Obviously, the first one seems to be the most energy-consuming because higher radius slices represent more material volume. However, between these two alternatives, any other $A(R)$ function has to be taken into account. Therefore the following relation has been chosen:

$$A(R) = R_0 + \frac{R_1/\sqrt{\lambda} - R_0}{R_1 - R_0}(R - R_0) + [1 - \exp(-\alpha(R - R_0))]\left[\frac{R_1}{R_1 - R_0}\frac{1 - 1/\sqrt{\lambda}}{\alpha} + \frac{\beta}{\alpha^2}\right] - \frac{\beta}{\alpha}(R - R_0)\exp(-\alpha(R - R_0)) \tag{8}$$

where α is the parameter to be optimized using the minimum energy principle and $\alpha \in [0; +\infty]$.

$$\beta = \frac{\gamma - 1}{\frac{1}{\alpha} + \frac{R_1 - R_0}{1 - \exp(\alpha(R_1 - R_0))}}$$

Then a point located at ($R \sin \theta$, $R \cos \theta$) moves to its new coordinates ($A(R) \sin \theta'$, $B(R) \cos \theta'$) in the

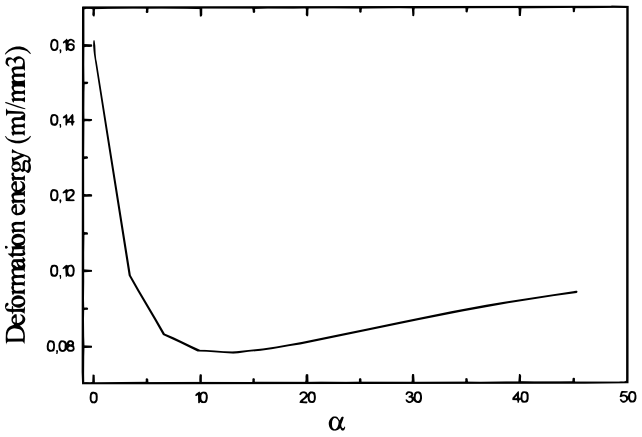

Figure 3. Deformation energy vs α for $\phi = 0.2$ and $\lambda = 1.3$.

undeformed state. θ' is calculated numerically using the following equation:

$$\theta = \arcsin \int_0^{\theta'} \frac{A(R)}{R^2} \cos x \, \Delta e \, \Delta s \, \mathrm{d}x \qquad (9)$$

where

$$\Delta e = \sqrt{\left(\frac{\mathrm{d}A}{\mathrm{d}R}(R) \cos x\right)^2 + \left(\frac{\mathrm{d}B}{\mathrm{d}R}(R) \sin x\right)^2} \times \cos\left(\arctan\left(\frac{\mathrm{d}B}{\mathrm{d}A}(R) \tan x\right) - \arctan\left(\frac{A(R)}{B(R)} \tan x\right)\right)$$

$$\Delta s = \sqrt{A^2(R) \sin^2 x + B^2(R) \cos^2 x}$$

Equation 9 arises from the conservation volume hypothesis (Appendix). One is now able to calculate the strain tensor at finite strain[10] within the elementary cell shell. However, it is relatively difficult to give an analytical solution of it. Therefore, it has been computed using the following procedure. The elementary cell shell is split into N torai. Using eqs 8 and 9, new coordinates of each torus can be calculated. Using a finite-element-like form function with four nodes, the strain tensor is computed at the center of the considered torus. The deformation energy of each torus is then computed and added to give the total deformation energy. However, the computed total deformation energy depends upon the strain field, which in turn is a function of α. Therefore, in order to find the most likely total deformation energy, one needs the optimum strain field, which corresponds to the optimum α value (α_{opt}). α_{opt} is simply computed using the minimum energy principle, which states that the most likely state corresponds to the less energy-consuming one. The optimum strain field is estimated by determining the α value that minimizes the mechanical energy. Figure 3 presents the deformation energy as function of α for $\lambda = 1.3$ and $\phi = 0.2$.

As can be seen, it is easy to find α_{opt}. However, when the macroscopic strain increases, α_{opt} has to be updated. Knowing α_{opt} for each λ, the strain-energy curve is then obtained for specific ϕ and shell strain-energy function.

Results. Based on these micromechanical calculations, one is able to investigate the uniaxial deformation of the elementary cell. The results presented below have been calculated using the Mooney−Rivlin equation[10] with $C_1 = 0.019$ and $C_2 = 0.14$ for the strain-energy function of the elementary cell shell. These Mooney−Rivlin coefficients C_1 and C_2 correspond to the initial mean strain rate (9.3×10^{-2} s^{-1}). However, any other strain-energy relation expressed as a function of the first and second strain invariants of the Green's strain tensor may be used.

The deformation of the elementary cell is described by three principal extension ratios: two in the (X, Z) plane (λ_1, λ_2) and one perpendicular to it (λ_3). Parts b−d of Figure 4 present the three principal extension ratio distributions within the elementary cell shell.

First of all, one may easily observe the strain amplification phenomenon in Figure 4b where the mean local strain is higher than the macroscopic strain. Furthermore, close to the elementary cell core, two different situations are occurring (Figure 4b,c). At the core pole and equator, λ_1 and λ_2 are almost equal to 1, which indicates no deformation in the (X, Z) plane. It is consistent with the hypothesis of perfect adhesion between the elementary cell core and shell. At the core pole and core equator, the shell material is experiencing mainly elongation and compression, respectively. However, since the shell volume is constant and the core undeformable, the shell material bounded to the core pole and equator cannot be deformed. The only way for the shell material bounded to the core to experience deformation is shearing, in order to satisfy the model hypothesis. At 45° with the deformation axis and close to the core, one may observe the highest values of both extension ratios. As shown in Figure 4a, that region is experiencing shearing strain for reasons explained previously. Away from the elementary cell core, one may observe a small extension ratio (equivalent to the macroscopic extension ratio) area at roughly 30° with the deformation direction.

Figure 4d presents results of the extension ratio λ_3 perpendicular to plane (X, Z). λ_3 corresponds to the ratio between a torus radius after and before deformation. It is therefore a parameter quantifying the "contraction" of shell torai. λ_3 is almost equal to 1 for shell bounded to the core. Comparing λ_3 of the two torai located at the same radius R but at different heights Z, one may observe that the higher the torus is located, the lower λ_3 will be. Torai are more "contracted" when they are located at a higher Z value. This is a consequence of the undeformable core hypothesis. The same explanation holds obviously for torai located at the same Z coordinate but a different R coordinate.

Three different strain rates describe as well the local strain rate of the elementary cell. However, dealing with uniaxial elongation, the common strain rate used corresponds to the first strain rate. It is of interest to compare the local first principal strain rate to the overall first strain rate (Figure 5).

Shell material bounded to the core pole and core equator has a zero strain rate because of the perfect core/shell adhesion hypothesis. The highest strain rate (5 times higher than the macroscopic strain rate) is experienced by shell material bounded to the core and located at 45° with the deformation axis. Away from the core, one may observe small strain rate (equivalent to the macroscopic strain rate) area. Eventually, the mean local strain rate is higher than the macroscopic strain rate, as predicted by the strain amplification phenomenon. The shell material deformation is therefore highly dependent upon its location within the film. For instance, the material bounded to the core is much more deformed and at a higher strain rate than any other part of the material.

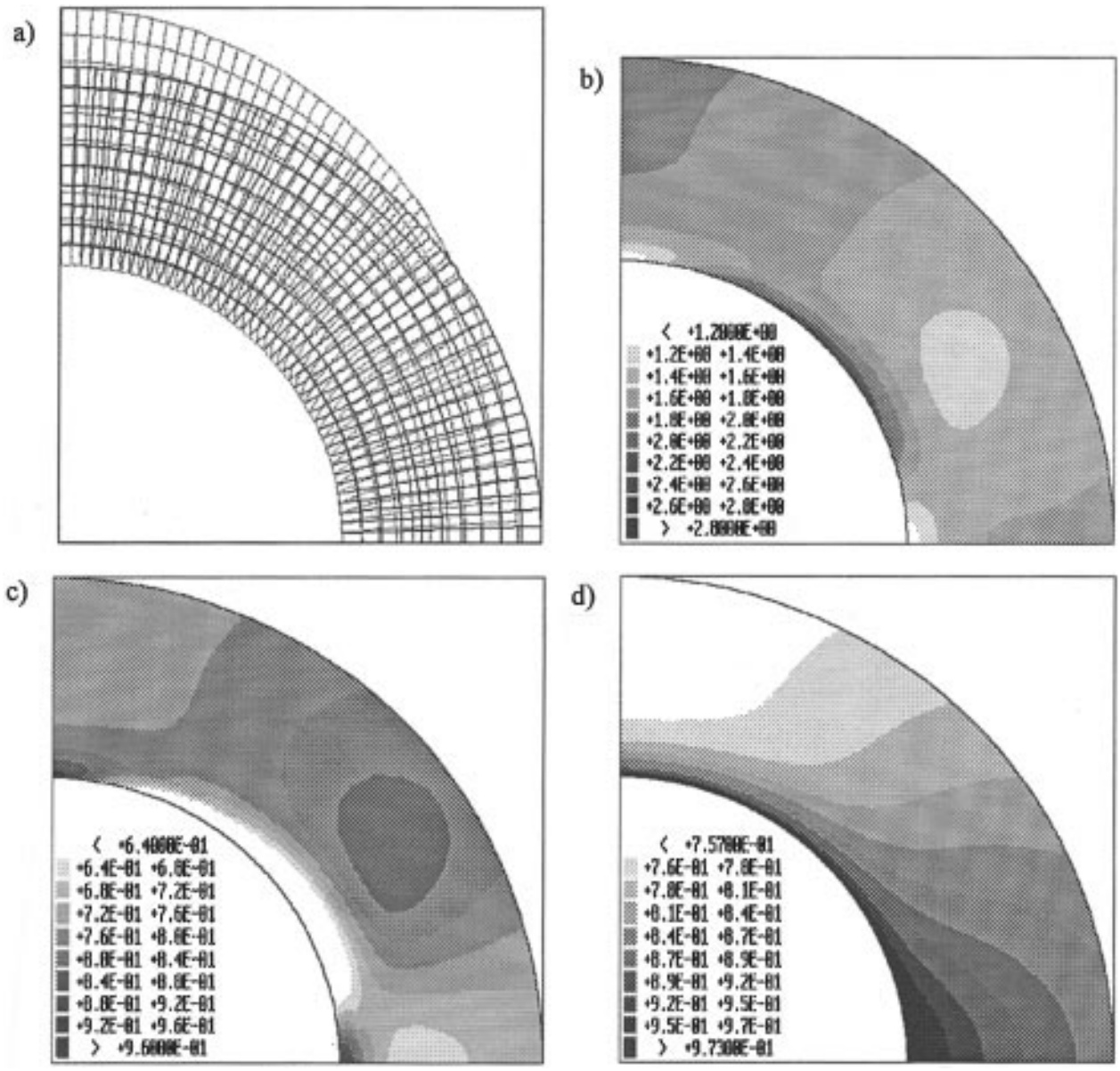

Figure 4. Results from the micromechanical model for $\lambda = 1.3$ and $\phi = 0.2$: (a) deformed and undeformed states; (b) first principal extension ratio distribution; (c) second extension ratio distribution; (d) third principal extension ratio distribution.

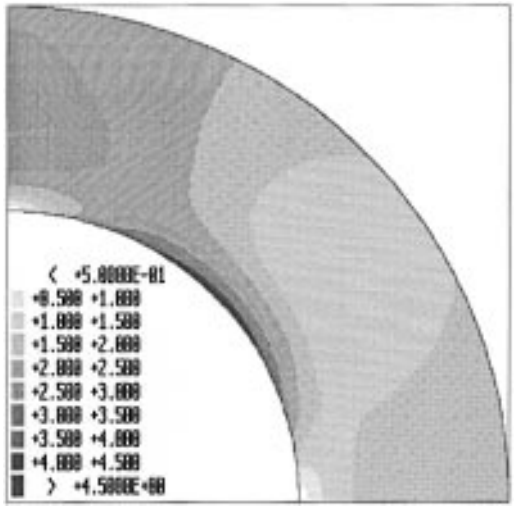

Figure 5. Local to macroscopic first principal strain rate ratio distribution calculated with the micromechanical model: $\lambda = 1.3$ and $\phi = 0.2$.

As mentioned earlier, shell material is not only deformed at different extension ratios but also at various strain rates. Therefore, if the shell material behavior is strain dependent, one has to take it into account during energy density computation. However, for reasons explained later (see Discussion in section III), the calculations presented herein assumed no strain rate dependence. Parts a and b of Figure 6 present the energy density distribution within the elementary cell shell.

It is clear in Figure 6a that the highest energy-consuming area is the one bounded to the core and located at 45° with the elongation direction. Furthermore, away from the elementary cell core a low energy-consuming zone may be observed. The same observations hold for higher strain, as shown in Figure 6b.

Knowing the total deformation energy as a function of macroscopic strain, it is easy to compare the strain−stress curves obtained by micromechanical calculations with experimental ones (Figure 7 to Figure 8). Core/shell latexes have been prepared by means of a two-step emulsion polymerization and dried under standard

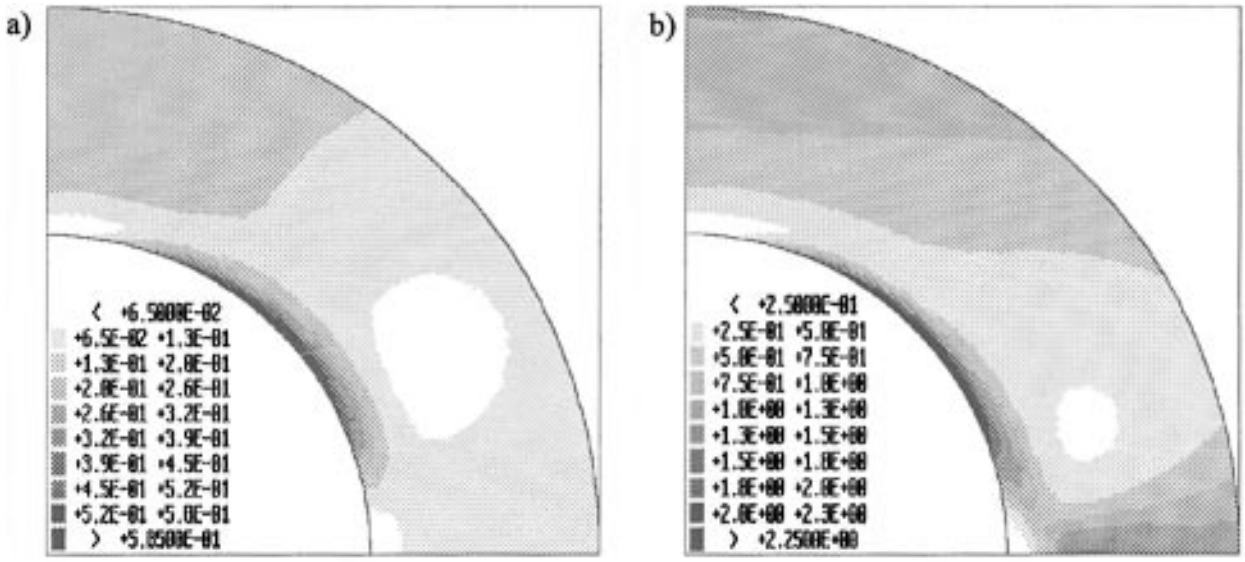

Figure 6. Energy density distribution calculated with micromechanical model for $\phi = 0.2$: (a) $\lambda = 1.3$; (b) $\lambda = 1.8$.

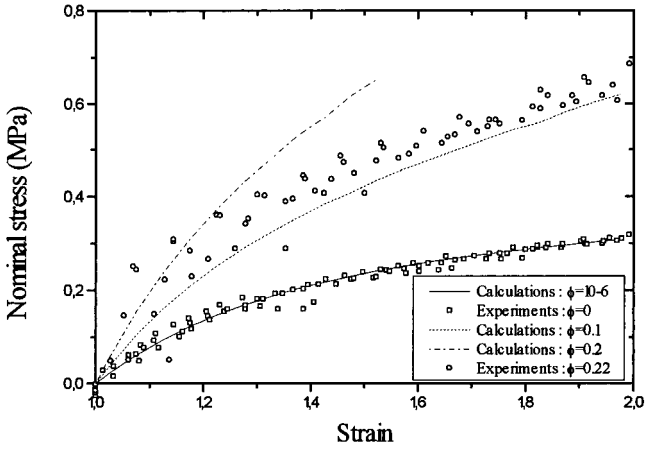

Figure 7. Experimental and calculated with the micromechanical model strain−stress curves. Crosshead speed = 200 mm/min.

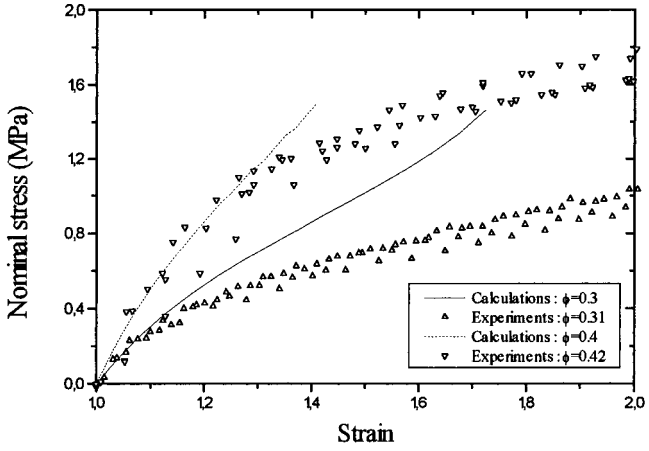

Figure 8. Experimental and calculated with the micromechanical model strain−stress curves. Crosshead speed = 200 mm/min.

conditions (23 °C, 60% relative humidity) for 25 days.[11] The core is based on poly(methyl methacrylate), and the shell is based on butyl acrylate−methyl methacrylate−acrylic acid copolymer ($T_g = -5$ °C). Film without inclusions was prepared from homogeneous latex particles based on the shell polymer. Uniaxial elongation experiments were eventually carried out at 200 mm/min.

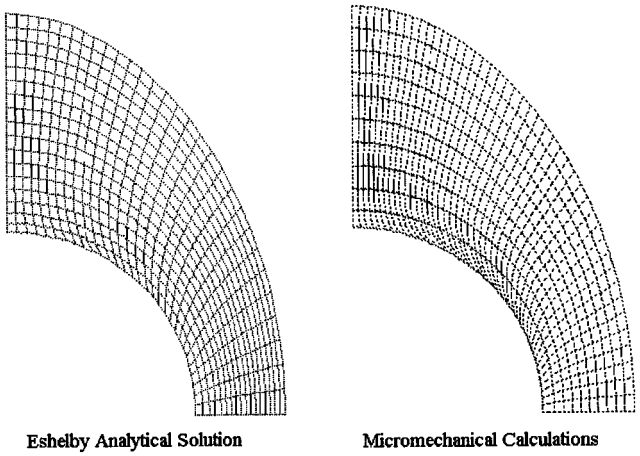

Figure 9. Deformed states calculated with the micromechanical model and the Eshelby analytical solution: $\lambda = 1.01$ and $\phi = 0.20$.

Figures 7 and 8 present comparisons between experimental and calculated data with micromechanical model strain−stress curves. For the sake of clarity, only a few experimental points are shown on these curves.

Although the agreement between experimental and calculated results is not perfect, one can be satisfied by such results because no adjustable parameter has been used. Furthermore, S-shaped stress−strain curves are also predicted. However, in every case the predicted curves are always above the experimental ones. Such result will be discussed later.

Discussion. Before discussing the previous results, it is interesting to look into the details of the main hypothesis of the micromechanical model, which is expressed by eq 8. By means of it, one may easily get the corresponding deformed state, but it is rather difficult to estimate experimentally its correctness. Using the autocoherent model, one may evaluate micromechanical kinematics correctness at least at small strain. Eshelby[12] in 1957 found the analytical solution for the deformation at small strain of a matrix containing ellipsoidal inclusions. It is therefore of interest to compare the deformed state obtained by the micromechanical model and the Eshelby solution at small strains. Such a comparison is presented in Figure 9.

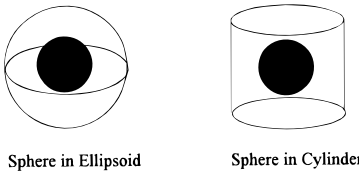

Figure 10. Elementary cells used for finite element calculations.

Figure 9 shows that deformed states obtained by micromechanical calculations and the Eshelby analytical solution are different. For instance, micromechanical calculations predict a higher shearing strain for the shell material bounded to the core cell than the Eshelby analytical solution does. On the other hand, the Eshelby analytical solution predicts a higher displacement of shell material located at the edge of the elementary cell than micromechanical calculations do. Although the Eshelby analytical solution is valid for small core volume fraction, such a comparison indicates that micromechanical calculation results have to be tested with another model, e.g., finite element, in order to be fully reliable.

III. Finite Element Calculations

Model Development. The alternative model used to study the mechanical behavior of coalesced core/shell latex films is based on the finite element method. Two different elementary cells have been used and are depicted in Figure 10.

The first one is based on a quasi-undeformable sphere surrounded by an elastomeric shell (sphere into ellipsoid), and the second one is based on the same quasi-undeformable sphere within an elastomeric cylinder (sphere into cylinder), the cylinder height being equal to its diameter. With the sphere into ellipsoid elementary cell, it is assumed that the ellipsoid principal axis is parallel to the deformation direction. Furthermore, in order to take into account neighbouring cells, it is assumed that points of the elementary cell surface located at θ with the deformation direction will keep their angles during the experiment. With the sphere into cylinder elementary cell, it is assumed that the cylinder edges remain vertical and that the top and the bottom of the cylinder keep their disklike shape during the experiment. Such boundary conditions are simple and conventionally used in finite elemental analysis.[13] The quasi-undeformable sphere mechanical properties have been taken equal to those of poly(methyl methacrylate) (Young modulus = 3000 MPa, Poisson coefficient = 0.4). The elastomeric material strain-energy function was defined by the Mooney−Rivlin equation with $C_1 = 0.019$ and $C_2 = 0.14$. Unfortunately, the software only allowed us to take into account the change of C_1 and C_2 with temperature but not with the strain rate. No attempt to suppress this limitation was made for reasons explained later on (see Discussion in section III). Finite element calculations were performed with ABAQUS software.

Results. From finite element results, one may obtain the spatial distribution of several parameters characterizing the deformation of the elementary cell. Parts a and b of Figure 11 present the energy density distribution obtained with the sphere in ellipsoid cell and sphere in cylinder cell.

As can be seen, the results are quantitatively similar to the ones obtained with the micromechanical model. The highest energy-consuming region of the elastomeric shell is the one located at 45° with the deformation direction and bounded to the core cell, while the lowest energy-consuming zone may be identified close the edge of the cell and located between 30 and 60° with the deformation direction.

The strain−stress curves may also be obtained by derivation of the total deformation energy. Figures 12 and 13 present the comparison between finite element calculations and experimental stress−strain curves (same experimental points as in Figures 7 and 8).

In both cases, the agreement between theoretical and experimental results is very good for the pure elastomer. However, the finite element analysis using the sphere in ellipsoid cell overestimates the experimental data. When the sphere in cylinder cell is used, the agreement between theoretical and experimental results is good for macroscopic extension ratio up to 1.2. But, for a higher macroscopic extension ratio the model overestimates the experimental data.

Discussion. Energy density distribution results obtained by finite element analysis have confirmed the ones obtained with the micromechanical model. These

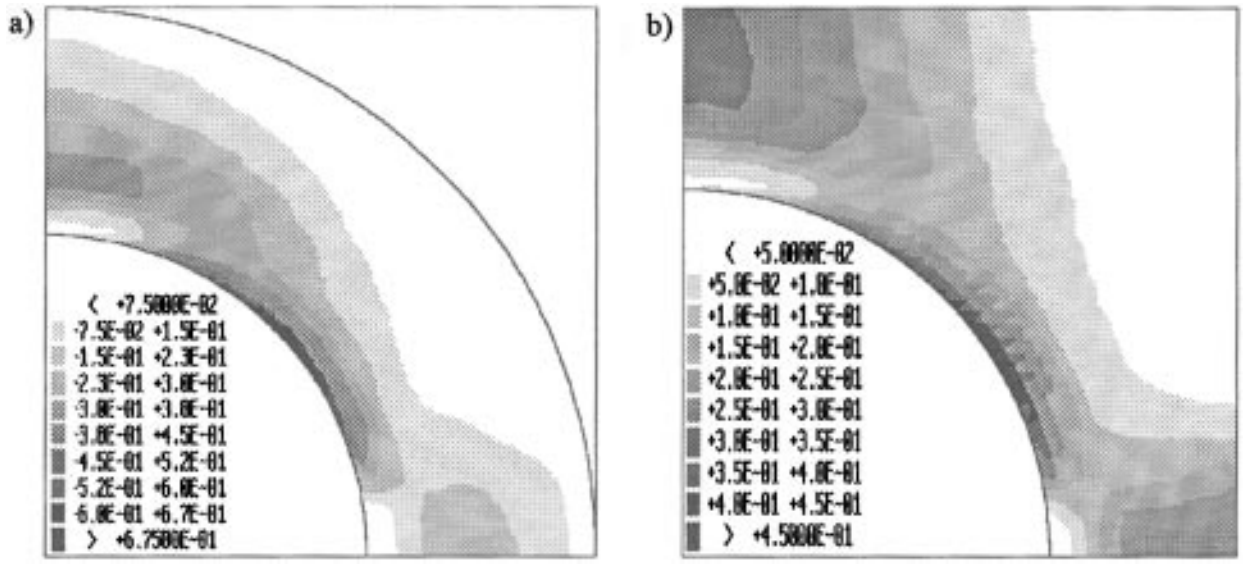

Figure 11. Energy density distribution calculated with finite element analysis for $\lambda = 1.3$ and $\phi = 0.20$: (a) using the sphere in ellipsoid cell; (b) using the sphere in cylinder cell.

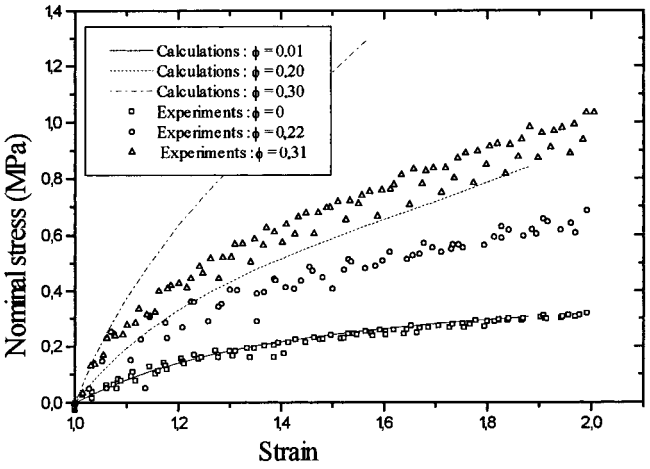

Figure 12. Experimental and calculated with the finite element analysis strain−stress curves using the sphere in ellipsoid cell.

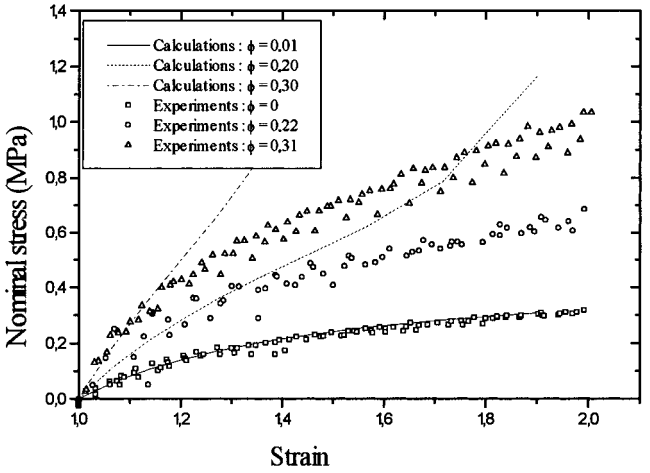

Figure 13. Experimental and calculated with the finite element analysis strain−stress curves using the sphere in cylinder cell.

results showed that the matrix material close to the core is experiencing higher deformation and at a higher strain rate than the rest of the matrix. Therefore, the important role of the matrix-inclusions interphase on mechanical properties of the core/shell film, and more generally of filled elastomer, is stressed by the presented results. It is even possible to conclude that the interphase is a favorable locus of fracture because of its high energy density. These theoretical conclusions confirm the well-known experimental results on mechanical behavior of filled elastomers.[14,15]

Comparison of experimental and calculated strain−stress curves has shown an interesting feature. Calculations overestimate experimental results in every case, although the finite element analysis using the sphere in cylinder cell gave good agreement for extension ratios up to 1.2. Three explanations may be proposed to elucidate such results.

Firstly, the molecular weight distribution (MWD) of the shell polymer in homogeneous films and films with inclusions may be different. It has been proved recently[16] that even homogeneous particles may have MWD spatial inhomogeneity. This phenomenon arises mainly from higher $\bar{n}$ (average number of radicals per particle) at the end of the polymerization than at the beginning. By comparing MWD of two latexes, the first one prepared by seeded emulsion polymerization (core/shell latex) and the other by unseeded emulsion polymerization (homogeneous latex), one may expect high $\bar{n}$ values (>1) all the polymerization long for the first latex type, and conventional $\bar{n}$ values (<0.5) for the second latex type. With vinyl acetate such observations have already been mentioned. Small $\bar{n}$ values (<0.5) were obtained for unseeded polymerization,[17] while high $\bar{n}$ values were estimated for seeded polymerization.[18] According to such considerations, the MWD of the shell polymer in the core/shell latex will be smaller than in the homogeneous latex. Since the mechanical behavior of the shell polymer is calculated from the homogeneous film, it may therefore be overestimated. However, it is very difficult to check such an explanation experimentally because specific extraction of the shell polymer in coalesced core/shell latex particles is almost impossible.

Secondly, the experiments were performed at constant crosshead speed. Therefore, the strain rate decreases during the experiment (eq 10), while strain rate is assumed constant in the calculations.

$$\dot{\epsilon} = \frac{1}{L}\frac{\nu}{1-\lambda}\ln\lambda \qquad (10)$$

where $\dot{\epsilon}$ is the strain rate (s^{-1}), L is the specimen length (mm), ν is the crosshead speed (mm/s), and λ is the extension ratio.

However, it has been shown previously (Figure 5) that the mean local strain rate is also higher than the macroscopic strain rate, because of the strain amplification phenomenon. For instance, the local strain rate is on average 2 times higher than the macroscopic strain rate for $\phi = 0.2$ and λ_1 close to 1. On the other hand, the strain rate decrease due to constant crosshead speed is only equal to 0.8 for $\lambda = 1.5$. Therefore, the overestimation of experimental results by models cannot be explained by the fact that the strain rate dependence was not included in the calculations.

Thirdly, the agreement between models and experiments is good for small strain. Since it is expected that any arbitrary kinematically admissible strain field overestimates the strain energy (demonstration has been established for small strain deformation[19]), one may assume that the kinematics used for the calculations seems to be close to the real one for strain below 1.2, but not for higher strain. Therefore, it can be surmised that a change of the kinematics occurs when the strain becomes higher than 1.2. Indeed, it has been mentioned that during calculations, the critical macroscopic extension ratio ($\lambda_{crit} = (R_1/R_0)^2$) is reached when the outer bound of the cell shell touches the surface cell core. A new kinematics, which has to be less energy consuming than the isotropic matrix deformation assumed in the presented calculations, has then to be devised before λ_1 becomes close to λ_{crit}. Therefore, it may be proposed that the deformation of a core−shell coalesced latex film proceeds through two simultaneous and/or successive kinematics: isotropic matrix deformation and geometrical core rearrangement in the film. The first mechanism should be dominant at smaller strain and/or low core/shell volume fraction and the second one should dominate at higher strain and/or high core/shell volume fraction. The proposed deformation mechanism is depicted in Figure 14.

IV. Conclusion

Film formation of (high T_g polymer-based core/film-forming polymer-based shell) latex particles gives rise to films having regularly distributed high modulus inclusions within an elastomeric matrix. The geo-

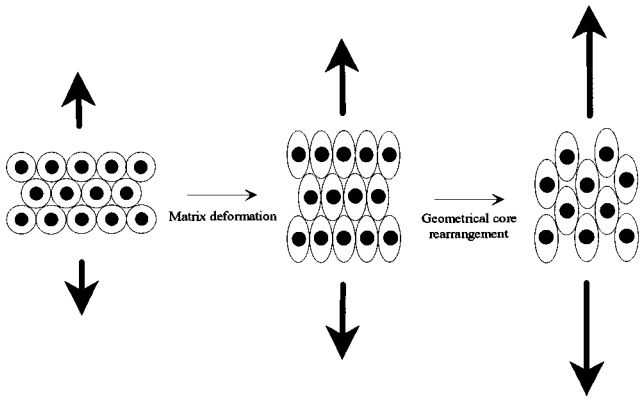

Figure 14. Proposed deformation mechanism of the coalesced core/shell latex films.

metrical periodicity of these films allowed one to model their mechanical behavior at finite strain based on elementary cell calculations. Two models were used and gave similar results. Firstly, the study of the energy density distribution showed that the matrix bounded to the inclusions is the highest energy-consuming region. Therefore, the matrix-inclusions interphase is likely the most favorable locus of fracture in core/shell coalesced latex films and special emphasis must be directed toward it in order to take advantage of such a situation. Secondly, experimental and calculated stress–strain curves have been compared. It was shown that a deformation mechanism based only on isotropic matrix deformation is too energy consuming to be responsible for the real biphasic film deformation. Therefore, it is proposed that uniaxial deformation of coalesced core/shell latex films proceeds through two simultaneous and/or successive mechanisms: isotropic matrix deformation and geometrical core rearrangement within the film. Such an explanation has been tested by looking at the surface of a deformed coalesced core/shell latex film using atomic force microscopy and is presented in the companion article. Eventually, although the mechanical model should be refined to take into account the increase of local stiffness with the microscopic strain rate, and so to attempt to estimate better the stress–strain curves, it appears that stiffening is mainly due to the mechanical effects. Moreover, the mechanical model gives an upper limit for the strain that corresponds to the beginning of the rearrangement of the cores.

Acknowledgment. The financial support from L'Oréal is gratefully acknowledged.

Appendix

A point located at ($R \sin\theta$, $R \cos\theta$) in the undeformed state moves to its new coordinates ($A(R) \sin\theta'$, $B(R) \cos\theta'$) after deformation. The volume of an elliptical slice between 0 and θ' is v_{def}, whereas the volume of a spherical slice between 0 and θ is v_{undef}.

The volume of an elliptical slice between 0 and θ' having $A(R)$ as the small principal axis and dA as the thickness is given by the following equation:

$$v_{def} = \int_0^{\theta'} 2\pi A(R) \cos x \, de \, ds$$

As schematically represented in Figure 15, ds is the derivative of the curvilinear abscissa whereas de is the thickness of the elliptical slice perpendicular to ds. One may then write

$$ds = \sqrt{A^2 \sin^2 x + B^2 \cos^2 x}\, dx$$

$$de = de' \cos\left(\arctan\left(\frac{dB}{dA}(R) \tan x\right) - \arctan\left(\frac{A(R)}{B(R)} \tan x\right)\right)$$

$$de' = \sqrt{\left(\frac{dA}{dR}(R) \cos x\right)^2 + \left(\frac{dB}{dR}(R) \sin x\right)^2}\, dR$$

Before deformation, one easily obtains the volume of the spherical slice between 0 and θ:

$$v_{undef} = \int_0^{\theta} 2\pi R \cos x \, dR \, R \, dx = 2\pi R^2 \sin\theta \, dR$$

θ' is then simply calculated numerically by equating v_{def} and v_{undef}.

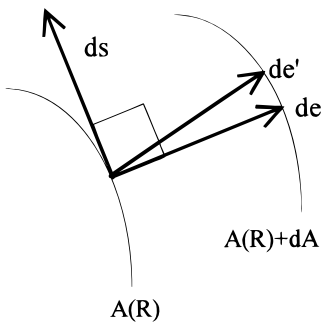

Figure 15.

References and Notes

(1) Vandezande, G. A.; Rudin, A. *J. Coat. Technol.* **1994**, *66*, (828), 99.
(2) Dickie, R. A.; Cheung, M. F. *J. Appl. Polym. Sci.* **1973**, *17*, 79.
(3) Mullins, L.; Tobin, N. R. *J. Appl. Polym. Sci.* **1965**, *9*, 2993.
(4) Mingshi, S.; Huanzhi, Z. *Polym. Bull.* **1987**, *17*, 63.
(5) Sato, T. *Int. Polym. Sci. Technol.* **1994**, *21* (3), 45.
(6) Winnick, M. A.; Yang, Y.; Haley, F. *J. Coat. Technol.* **1992**, *64* (811), 51.
(7) Joanicot, M.; Wong, K.; Maquet, J.; Chevalier, Y.; Pichot, C.; Graillat, C.; Linder, P.; Rios, L.; Cabane, B. *Prog. Colloid Polym. Sci.* **1990**, *81*, 175.
(8) Sosnowski, S.; Li, L.; Winnick, M. A.; Clubb, B.; Shivers, R. *J. Polym. Sci., Part B* **1994**, *32*, 2499.
(9) Aklonis, J. J.; MacKnight, W. J.; Shen, M. *Introduction to Polymer Viscoelasticity*; Wiley-Interscience: New York, 1972; Chapter 2.
(10) Ward, I. M. *Mechanical Properties of Solid Polymers*; 2nd ed.; Wiley: New York, 1983; Chapter 3.
(11) Lepizzera, S. Ph.D. Thesis, Strasbourg University, 1995.
(12) Eshelby, J. D. *Proc. R. Soc.* **1957**, *A241*, 376.
(13) Guild, J.; Young, R. J.; Lovell, P. A. *J. Mater. Sci.* **1994**, *13*, 10.
(14) Kraus, G. In *Science and Technology of Rubber*; Eirich, F. R., Ed.; Academic Press: New York, 1978; Chapter 8, p 339.
(15) Bourgeat-Lami, E.; Espiart, P.; Guyot, A.; Briat, S.; Gauthier, C.; Vigier, G.; Perez, J. A. C. S. Symposium Series, In *Hybrid Organic-Inorganic Composites*; Mark, J. E., Lee, C. Y. C., Bianconi, P. A., Eds.; American Chemical Society: Washington, DC, 1994; Chapter 10, p 585.
(16) Clay, P. A.; Gilbert, R. G. *Multi-Phase Materials prepared by Emulsion Polymerization*; Lancaster: England, 1995.
(17) Nomura, M.; Harada, M.; Nakagawara, K.; Eguchi, W.; Nagata, S. *J. Chem. Eng. Jpn.* **1971**, *4* (2), 48.
(18) Lepizzera, S.; Hamielec, A. E. *Makromol. Chem. Phys.* **1994**, *195*, 3103.
(19) François, F.; Pineau, A.; Zaoui, A. *Comportement mécanique des matériaux*; Hermes: Paris, 1991; Vol. 1, Chapter 2.

MA960729L